Modeling the Tensile Behavior of Ultra-High-Molecular-Weight Polyethylene with a Novel Flow Rule

J. Sweeney, S. Naz, P. D. Coates

School of Engineering, Design and Technology/Interdisciplinary Research Center in Polymer Science and Technology, University of Bradford, Bradford BD7 1DP, United Kingdom

Received 11 May 2010; accepted 22 November 2010
DOI 10.1002/app.33844
Published online 30 March 2011 in Wiley Online Library (wileyonlinelibrary.com).

ABSTRACT: A study of the tensile behavior of ultra-high-molecular-weight polyethylene over a range of strain rates showed that its strain rate sensitivity was a function of the strain. This was related to a flow rule developed for this material in a previous study on compressive behavior. This flow rule is an adaptation of that of Hill, in which the anisotropy coefficients are power-law functions of the extension ratios. It is used in conjunction with an Eyring process. The observed rate dependence of the tensile behavior conformed with that obtained with the power-law flow rule and could be used to derive a value of the power-law coefficient. Independent observations were made of the relationship between the axial and transverse strains in tensile specimens with inhomogeneous strain fields. A constitutive model was developed that incorporates the new flow rule and was implemented in a finite element analysis. When this analysis was used to model the inhomogeneous tensile specimens, it gave predictions of the axial and transverse strain that were consistent with the experiment when the power-law coefficient was the same value as that derived from the study of the rate dependence. © 2011 Wiley Periodicals, Inc. J Appl Polym Sci 121: 2936–2944, 2011

Key words: mechanical properties; strain; stress; tension

INTRODUCTION

Ultra-high-molecular-weight polyethylene (UHMWPE) continues to be of importance as a structural material. As a result, its constitutive behavior has been studied extensively and represented by complex models.[1–3] In service, the material can be subjected to multiaxial strain fields, and it is desirable that this should be reflected in any program of experimental verification. In a previous study,[4] we investigated its constitutive behavior when it was subjected to compressive strain in both the uniaxial and nonuniaxial modes. A constitutive theory was developed that gave an adequate representation of the experimental data. We found that an unconventional flow rule, featuring strain-induced anisotropy, was essential to the realistic functioning of the constitutive model, particularly in the representation of the nonuniaxial (plane strain) results. The particular form adopted for anisotropy was a power-law dependence on the principal extension ratios. In this study, we extended this work to tensile behavior.

The purpose of this study was to explore whether a flow rule similar to that required for compression is necessary in the case of tension. The plane strain experiments that proved crucial in the interpretation of compressive behavior were found to be not practically possible in tension. However, we found that the issue of the flow rule could be successfully addressed via a program of experiments that included both uniform and nonuniform tension, together with a detailed study of the dependence of the strain rate sensitivity on strain. We concluded that a flow rule of the type derived for compressive behavior continued to give a performance for tensile stretching far superior to that of the conventional Lèvy-Mises rule.

EXPERIMENTAL

In all tests, UHMWPE (grade GUR1050) was used; it was manufactured by Hoechst and supplied by Orthoplastics (Lancashire, United Kingdom) in the form of compression-molded blocks. The molar mass of this grade of polymer has been estimated in the range 5.5–6.0 $\times$ 10^6 g/mol with intrinsic viscosity measurements.[5] The crystallinity of the sample was determined at a value of 40.96% as quantified with modulated differential scanning calorimetry with experimental details, as specified previously.[4]

Uniaxial tests were carried out in tension with an Instron testing machine (model 5568, Instron Ltd. High Wycombe UK) operating at room temperature. To determine the stress–strain behavior under uniform strain conditions, the tensile specimen geometry shown in Figure 1(a) was used; it was based on a

Correspondence to: J. Sweeney (j.sweeney@bradford.ac.uk).

Contract grant sponsor: Engineering and Physical Sciences Research Ccouncil (to S.N. for a student-ship).

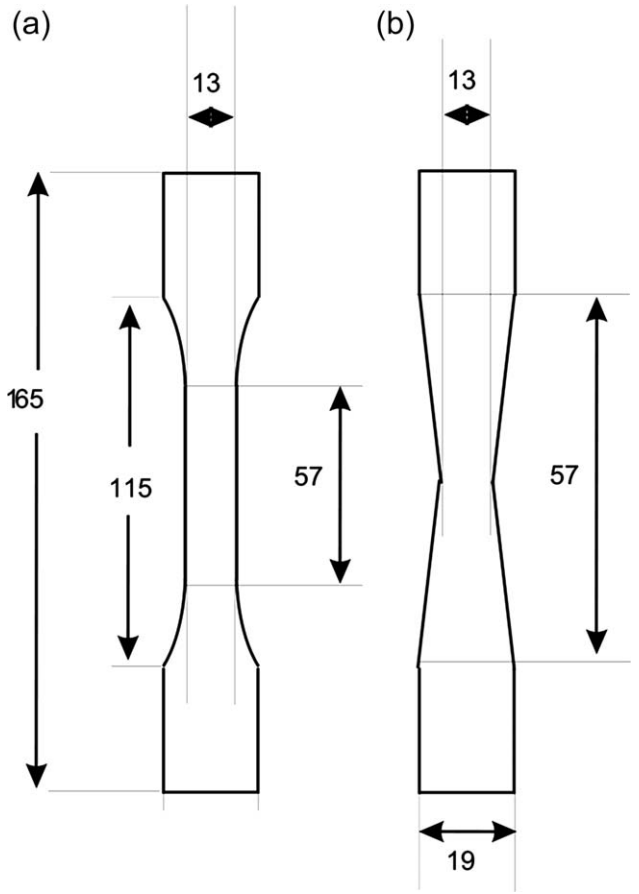

Figure 1 Tensile specimens: (a) 5 mm thick and (b) with nonuniform strain field and 1 mm thick. Dimensions are in millimeters.

type I ASTM D 638 standard. The strains were measured with the aid of a video extensometer (MessPhysik ME46NG, Messphysik Materials TestingGMBH Furstenfeld Austria), which sensed the separation of two parallel pen lines 50 mm apart on the 75-mm parallel gauge length. Tests were carried out at constant speeds; this resulted in approximately constant rates of the engineering strain in the range 0.005–0.08 s^{-1}. The strain fields remained uniform throughout the tests, with no signs of necking. Nonuniform strain fields were also explored with tensile tests of the geometry shown in Figure 1(b). A single testing speed was used and corresponded to an initial overall strain rate of 0.015 s^{-1}. Deformation fields in the form of arrays of dots printed on the specimens were captured with a Sony Handycam 6.1 MP digital video camera operating at 25 frames/s.

CONSTITUTIVE MODELING

An essential element of the theory is a series combination of an elastic element and an Eyring process. To form the model, this combination is placed in parallel with a hyperelastic element; the series combination arm of the model is assigned the superscript X, and the hyperelastic arm of the model is assigned the superscript Y. To allocate the strain between the elastic and plastic elements in the combination arm, we split the deformation gradient ($\mathbf{F}$) multiplicatively into elastic and plastic components ($\mathbf{F^e}$ and $\mathbf{F^p}$, respectively):

$$\mathbf{F} = \mathbf{F^e F^p} \tag{1}$$

Our method conformed to that classified by Figiel and Buckley,[6] as approach II, case 2′. Here, we assumed that all of the rigid body rotation was included in the plastic deformation. $\mathbf{F^p}$ was thus split into pure deformation ($\mathbf{V^p}$) and rigid body rotation ($\mathbf{R}$; via the use of the Cauchy–Green strain measure) to give the following:

$$\mathbf{F^p} = \mathbf{V^p R} \tag{2}$$

$\mathbf{F^e}$ was symmetric, with $\mathbf{F^e} = \mathbf{V^{eX}}$, the elastic strain in the combination arm, so that eq. (2) became

$$\mathbf{F} = \mathbf{V^{eX} V^p R} \tag{3}$$

An incremental approach was used, with strain rate assumed to be constant during each time increment. The current plastic stretch ($\mathbf{V^p}$) was related to the plastic strain at the end of the previous time increment ($\mathbf{V_0^p}$) and the increment of plastic strain ($\Delta\mathbf{V^p}$) developed during the current increment, by the following relation:

$$\mathbf{F} = \mathbf{V^{eX}} \Delta\mathbf{V^p V_0^p R} \tag{4}$$

$\mathbf{V^{eX}}$ and $\Delta\mathbf{V^p}$ are collinear, with $\Delta\mathbf{V^p}$ related directly to the derivative $\dot{\mathbf{V}}^{\mathbf{p}}$ via the time increment.

$\Delta\mathbf{V^p}$ results from the scalar plastic strain rate ($\dot{e}_{\mathbf{p}}$) generated by the Eyring equation

$$\dot{e}_p = A \exp\left(V_p \bar{\sigma}\right) \sinh(V_s \tau) \tag{5}$$

where A, V_p, and V_s are material constants, with the latter two being proportional to pressure and shear activation volumes, respectively (following, e.g., Buckley and Jones[7] or Spathis and Kontou[8]); $\overline{\sigma}$ is the mean stress, and τ is the driving stress and is defined later, in eq. (9). We defined $\dot{e}_p$ in terms of the plastic strain rate tensor ($\mathbf{L^p}$):

$$\dot{e}_p = \sqrt{\frac{1}{3}\mathbf{L^p}\mathbf{:}\,\mathbf{L^p}} \tag{6}$$

which is itself defined in terms of $\mathbf{L^p}$ by

$$\mathbf{L^p} = \dot{\mathbf{V}}^{\mathbf{p}} \mathbf{V^{p-1}} \tag{7}$$

To define the components of the plastic strain rate, we adapted the Hill criterion[9] for anisotropic yielding for the arbitrary axes 1, 2, and 3:

$$\begin{aligned}
\mathbf{L}^{\mathbf{p}}_{\mathbf{11}} &= \dot{e}_p[H(\sigma_{11}-\sigma_{22})+G(\sigma_{11}-\sigma_{33})]/3\tau \\
\mathbf{L}^{\mathbf{p}}_{22} &= \dot{e}_p[F(\sigma_{22}-\sigma_{33})+H(\sigma_{22}-\sigma_{11})]/3\tau \\
\mathbf{L}^{\mathbf{p}}_{33} &= \dot{e}_p[G(\sigma_{33}-\sigma_{11})+F(\sigma_{33}-\sigma_{22})]/3\tau \\
\mathbf{L}^{\mathbf{p}}_{23} &= \dot{e}_p L\sigma_{23}/3\tau \\
\mathbf{L}^{\mathbf{p}}_{13} &= \dot{e}_p M\sigma_{13}/3\tau \\
\mathbf{L}^{\mathbf{p}}_{12} &= \dot{e}_p N\sigma_{12}/3\tau
\end{aligned} \tag{8}$$

where σ is the stress and F, G, H, L, M, and N are anisotropy parameters. Equation (8) represents the incompressible plastic flow. From the definition in eq. (6) of $\dot{e}_p$, it follows that τ is given by

$$\tau = \frac{1}{3}\left[\frac{1}{3}\left\{[H(\sigma_{11}-\sigma_{22})+G(\sigma_{11}-\sigma_{33})]^2+[F(\sigma_{22}-\sigma_{33}) +H(\sigma_{22}-\sigma_{11})]^2+[G(\sigma_{33}-\sigma_{11})+F(\sigma_{33}-\sigma_{22})]^2+2[L^2\sigma_{23}^2+M^2\sigma_{23}^2+N^2\sigma_{12}^2]\right]^{1/2} \tag{9}$$

When $F = G = H = L = M = N = 1$, eq. (8) is equivalent to the Lèvy–Mises flow rule. When the anisotropy is strain induced, the anisotropy parameters are initially unity. The principal planes of orthotropy are subsequently determined by the strains. It has been concluded[4] that the total strain, rather than the elastic strain, provides the most effective model; hence, the parameters F, G, H, L, M, and N are functions of the total strain ($\mathbf{V^{eX}V^{p}}$). The principal directions of orthotropy at each point are, thus, the eigenvectors of $\mathbf{V^{eX}V^{p}}$ associated with the principal extension ratios (λ_{I}, λ_{II}, and λ_{III}). In the axis set 1′, 2′, and 3′ coinciding with these principal axes, we defined the anisotropy parameters (F', G', and H') using a power-law model as done previously:[4]

$$\begin{aligned}
F' &= \lambda_{\mathrm{I}}^m \\
G' &= \lambda_{\mathrm{II}}^m \\
H' &= \lambda_{\mathrm{III}}^m
\end{aligned} \tag{10}$$

where the exponent m is a material parameter. The shear terms (L', M', and N') were derived by transformation of the appropriate stress and strain fields into a state of pure shear:

$$\begin{aligned}
L' &= \frac{1}{2}(G'+H') \\
M' &= \frac{1}{2}(F'+H') \\
N' &= \frac{1}{2}(F'+G')
\end{aligned} \tag{11}$$

The anisotropy parameters in any other axis set could be derived from those defined in eqs. (10) and (11) by the appropriate fourth-order transformation.[10] A two-dimensional plane stress approach was adopted. In the 1′–2′ plane, eq. (8) becomes

$$\begin{aligned}
\mathbf{L}^{\mathbf{p}}_{\mathbf{1'1'}} &= \dot{e}_p[(G'+H')\sigma_{1'1'}-H'\sigma_{2'2'}]/3\tau \\
\mathbf{L}^{\mathbf{p}}_{\mathbf{2'2'}} &= \dot{e}_p[(F'+H')\sigma_{2'2'}-H'\sigma_{1'1'}]/3\tau \\
\mathbf{L}^{\mathbf{p}}_{\mathbf{1'2'}} &= \dot{e}_p[F'+G']\sigma_{1'2'}/6\tau
\end{aligned} \tag{12}$$

For an axis set 1^θ–2^θ at angle θ to the 1′–2′ axes, the equations equivalent to those in eq. (12) were obtained by introduction of the coefficients I^θ, J^θ and K^θ:

$$\begin{aligned}
I^\theta &= (G'+H')\cos^4\theta - 2H'\sin^2\theta\cos^2\theta \\
&\quad + (F'+H')\sin^4\theta + 2(F'+G')\sin^2\theta\cos^2\theta \\
J^\theta &= (F'+H')\cos^4\theta - 2H'\sin^2\theta\cos^2\theta \\
&\quad + (G'+H')\sin^4\theta + 2(F'+G')\sin^2\theta\cos^2\theta \\
K^\theta &= (F'+2H'+G')\sin^2\theta\cos^2\theta - H'\left(\sin^4\theta+\cos^4\theta\right) \\
&\quad - 2(F'+G')\sin^2\theta\cos^2\theta
\end{aligned} \tag{13}$$

so that the analogue of (12) in the rotated axis set was

$$\begin{aligned}
\mathbf{L}^{\mathbf{p}}_{\mathbf{1^\theta 1^\theta}} &= \dot{e}_p\left[I^\theta\sigma_{1^\theta 1^\theta}-K^\theta\sigma_{2^\theta 2^\theta}\right]/3\tau \\
\mathbf{L}^{\mathbf{p}}_{\mathbf{2^\theta 2^\theta}} &= \dot{e}_p\left[J^\theta\sigma_{2^\theta 2^\theta}-K^\theta\sigma_{1^\theta 1^\theta}\right]/3\tau \\
\mathbf{L}^{\mathbf{p}}_{\mathbf{1^\theta 2^\theta}} &= \dot{e}_p\left[I^\theta+J^\theta-2K^\theta\right]\sigma_{1^\theta 2^\theta}/3\tau
\end{aligned} \tag{14}$$

The elastic element in the combination arm was assumed to be a single-term Ogden model with exponent n_X. The stresses were defined by the elastic extension ratios, which were the eigenvalues of $\mathbf{V^{eX}}$, denoted by λ_{IV}, λ_{V}, and λ_{VI}, defined in the axis set IV–V–VI. In this two-dimensional analysis, the VI axis coincided with the 3 and 3′ axes. Because the Ogden model includes the assumption of incompressibility, $\lambda_{\mathrm{VI}} = 1/\lambda_{\mathrm{IV}}\lambda_{\mathrm{V}}$, and the principal stresses in the plane are given by the following:

$$\begin{aligned}
\sigma_{\mathrm{IV}} &= C_X\left[\lambda_{\mathrm{IV}}^{n_X}-(\lambda_{\mathrm{IV}}\lambda_{\mathrm{V}})^{n_X}\right] \\
\sigma_{\mathrm{V}} &= C_X\left[\lambda_{\mathrm{V}}^{n_X}-(\lambda_{\mathrm{IV}}\lambda_{\mathrm{V}})^{n_X}\right]
\end{aligned} \tag{15}$$

where C_X is a material constant.

The values of $\mathbf{V^{eX}}$ and $\Delta\mathbf{V^{p}}$ in eq. (4) were derived via an iterative process to impose the condition that the elastic stress and that in the Eyring process were equal, whereas the strains in the two elements were related to the total strain by eq. (4). At each iteration, stresses were generated with eq. (15) to drive the Eyring process via eqs. (9)–(14). The values of the plastic and elastic strain components were adjusted until the stresses in the two processes, having been transformed onto a common axis set via the use of eqs. (13) and (14), were sufficiently close. The resulting true stress was then transformed to global directions 1–2 to give the stress tensor $\Sigma^{\mathbf{X}}$. Finally, the plastic strain tensor ($\mathbf{V^{p}}$) at the end of the time increment was the symmetric part of $\mathbf{F^{p}}$ with

$$\mathbf{F^{p}} = \Delta\mathbf{V^{p}}\mathbf{V_0^{p}}\mathbf{R} = \mathbf{V^{p}}\mathbf{R}' \tag{16}$$

where, in general, the rigid body rotation ($\mathbf{R}'$) is through a different angle differs from $\mathbf{R}$.

The principal stresses in the hyperelastic arm were defined with an Ogden model with exponent n_Y. The strains in the hyperelastic arm were identical to the total strain ($\mathbf{V^{eX}V^{p}}$) corresponding to principal extension ratios λ_{I}, λ_{II}, and λ_{III}, to give principal stresses as follows:

$$\begin{aligned}\sigma_{\mathrm{I}} &= C_Y\left[\lambda_{\mathrm{I}}^{n_Y} - (\lambda_{\mathrm{I}}\lambda_{\mathrm{II}})^{n_Y}\right]\\ \sigma_{\mathrm{II}} &= C_Y\left[\lambda_{\mathrm{II}}^{n_Y} - (\lambda_{\mathrm{I}}\lambda_{\mathrm{II}})^{n_Y}\right]\end{aligned} \tag{17}$$

where C_Y is a material constant.

When transformed to global directions, they yielded the stress tensor $\Sigma^{\mathbf{Y}}$. The total stress (Σ) is then given by

$$\Sigma = \Sigma^{\mathbf{X}} + \Sigma^{\mathbf{Y}} \tag{18}$$

This analysis was programmed as a UMAT subroutine in the finite element package ABAQUS 6.8 (Simulia Providence RI).

STRAIN RATE DEPENDENCE OF STRESS

The strong nonlinearity of the Eyring process gave rise to yielding behavior when the rate of strain applied to the material became equal to the Eyring plastic strain rate.[11] The yield stresses predicted by the Eyring model were strain rate dependent, with an approximately linear relationship between the logarithm of the strain rate and the yield stress. When the flow rule discussed here was included in the analysis, the gradient of the linear relationship, the strain rate sensitivity, was predicted to be dependent on strain.

Here, we explore this effect for uniaxial conditions. The 1–2–3, 1′–2′–3′, and I–II–III axis sets coincided and set $\sigma_{11} = \sigma$ and all other stress components to zero. The first equation of eq. (12) gives for the plastic strain rate along I:

$$\frac{\dot{\lambda}_{\mathrm{I}p}}{\lambda_{\mathrm{I}p}} = \sqrt{2}\dot{e}_p \tag{19}$$

With eq. (10), τ [eq. (9)] becomes

$$\tau = \frac{\sqrt{2}}{3}\sigma\lambda_{\mathrm{I}}^{-m/2} \tag{20}$$

We then used eq. (5). In the customary way,[11] we assumed a large argument in the hyperbolic sine function so that it could be approximated by an exponential:

$$\dot{e}_p = \frac{1}{2}A\exp\left[V_p\bar{\sigma} + V_s\tau\right] \tag{21}$$

With the knowledge that for uniaxial conditions, $\overline{\sigma} = \sigma/3$ and with eqs. (19) and (20), this may be re-expressed as

$$\sigma = \left(\frac{3}{V_p + \sqrt{2}V_s\lambda_{\mathrm{I}}^{-m/2}}\right)\left[\ln\left(\frac{\dot{\lambda}_{\mathrm{I}p}}{\lambda_{\mathrm{I}p}}\right) - \ln\left(\frac{A}{\sqrt{2}}\right)\right] \tag{22}$$

which shows a linear relationship between the stress and logarithmic plastic strain rate, with a gradient that depends on the strain. This relation may be used to analyze experimental data when it is assumed that the experimental strain rate can be equated with the plastic strain rate, that is, at the yield point. It may also be useful when this is only approximately the case, as shown later.

RESULTS AND ANALYSIS

A typical experimental stress–strain curve at an intermediate strain rate of 0.018 s^{-1} is shown in Figure 2, showing as salient features the initial linear response, followed by yieldlike behavior, and finally, strain hardening. In quantitative terms, curves such as these depend on the rate of strain. The results of an analysis of the strain rate dependence for five rates in the range 0.005–0.08 s^{-1} are summarized in Figure 3. Here, stress is plotted as a function of the logarithm of strain rate, in a manner suggested by eq. (22), for a number of fixed strains. The stresses were approximated quite well by the linear function of logarithmic strain rate, and there was a clear trend of increasing gradient with increasing strain. The values of strain plotted were well beyond the yield strain, and so we were confident that the elastic strain rate was very small in comparison with the plastic strain rate. The total applied strain rate, being the sum of the elastic and plastic components, could

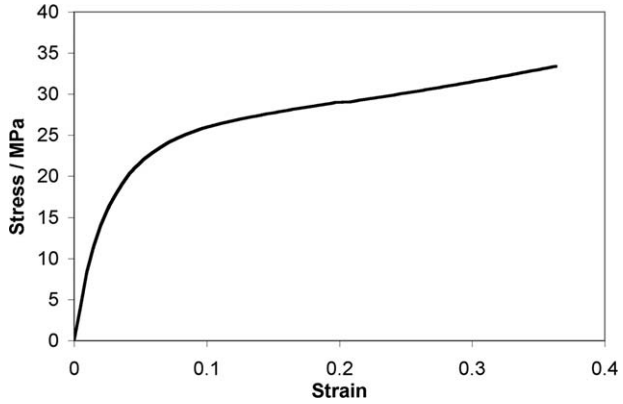

Figure 2 Tensile stress–strain curve at strain rate 0.018 s^{-1}.

then be equated with the plastic strain rate, and we used eq. (22) to analyze the results.

According to eq. (22) the gradient (g) of the stress–logarithm of the strain rate plot is given by

$$g = \frac{3}{V_p + \sqrt{2}V_s\lambda_I^{-m/2}} \tag{23}$$

To interpret the observed strain dependence of g in terms of eq. (23), we made use of the observation for this material that $V_p = 0.13V_s$.[12] This was based on the relationship between the observed tensile and compressive uniaxial stress–strain behavior. The values of g from Figure 3 are plotted against strain in Figure 4, together with the following function:

$$g = \frac{3}{V_s\left(0.13 + \sqrt{2}\lambda_I^{-m/2}\right)} \tag{24}$$

for various combinations of V_s and m. The slope of g in Figure 4 is dominated by the value of m, with changes in V_s resulting in vertical shifting. It was clear that a value of $m \approx 5$ gave a good representation of the observed strain dependence of g. The values of V_s corresponding to the m values used to calculate the fitted lines in Figure 4 are given in Table I.

This argument presupposed that V_s was constant for any given m and that it was the flow rule, via the factor $\lambda_I^{-m/2}$ in eq. (24), that caused the strain rate sensitivity to depend on the strain. Another possibility is that V_s itself depends on the strain. Additional experimental observations are necessary to separate the two possible sources of strain dependence. In compressive studies, plane strain experiments were used to make more explicit observations of the effects of the flow rule.[4] Although this type of experiment has not proven to be practically feasible in tension, an alternative in the form of tensile tests using the specimen geometry of Figure 1(b) proved useful. The effect of the nonuniform stress field is that the regions of the specimen under low stress imposed lateral restraints on the more highly stressed regions of the specimen and affected the lateral contraction in a way that depended on the flow rule and the exponent m. The effect was quantified with finite element modeling.

The theory outlined previously under the Constitutive Modeling section was implemented within the ABAQUS 6.8 commercial code. The finite element mesh of a quarter of the specimen of the type shown in Figure 1(b) is shown in Figure 5, where the lower horizontal and left-hand vertical boundaries are symmetry boundaries. In Figure 6, we show an image of a specimen, displaying the pattern of dots printed on it to aid strain analysis. We characterized the specimen deformation by measuring two perpendicular mean strains ($\bar{\varepsilon}$s): the average transverse strain along the horizontal symmetry axis at the specimen center ($\bar{e}_1$) and the average strain on the

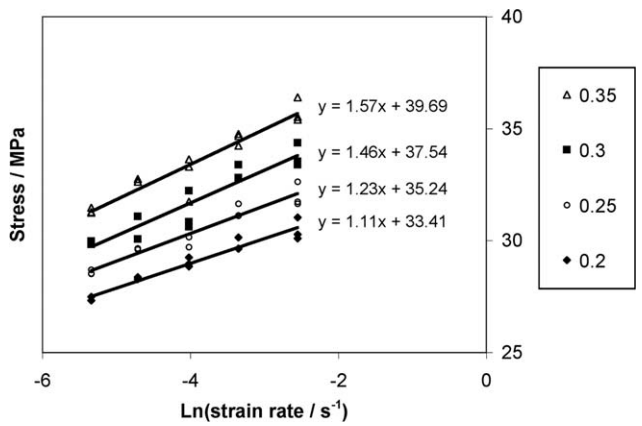

Figure 3 Strain rate dependence at four levels of strain.

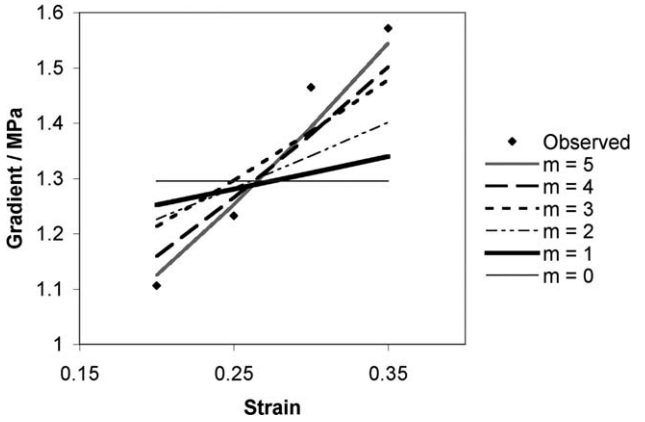

Figure 4 Fits to strain rate dependence for various power-law exponents.

TABLE I
Material Parameters

m	V_s (MPa^{-1})	V_p (MPa^{-1})	A (s^{-1})	C_X (MPa)	n_X	C_Y (MPa)	n_Y
0	1.5	0.195	3.2×10^{-10}	272	2	7.0	2
1	1.7	0.221	1.3×10^{-11}	272	2	3.7	2
2	1.9	0.247	1.3×10^{-11}	136	4	3.7	2
3	2.1	0.273	1.4×10^{-12}	90.7	6	1.0	2
4	2.4	0.312	1.4×10^{-12}	68	8	1.0	2
5	2.7	0.362	1.9×10^{-13}	54	10	0.0	2

vertical symmetry axis between two dots either side of the horizontal symmetry axis ($\bar{e}_2$), as illustrated in Figure 6. These quantities are defined in terms of the initial point separation (L) and the separation (ℓ) after deformation as follows:

$$\bar{e} = \ln(\ell/L) \tag{25}$$

The equivalent model predictions were derived from appropriate nodal displacements, and comparison was made via the strain ratio (R), where

$$R = -\frac{\bar{e}_1}{\bar{e}_2} \tag{26}$$

The finite element analysis was run for a number of values of the power-law exponent m. For each value of m, the value of V_s was that required to generate the values of g plotted in Figure 4, whereas, as noted previously, $V_p = 0.13V_s$. Other model parameters were chosen so that realistic stress–strain curves were generated. Examples of these curves for the strain rate 0.018 s^{-1} are shown in Figure 7, and the parameter values are listed in Table I. The parameter A was fixed such that the magnitude of the predicted yield stress corresponding to an abrupt change in the slope of the curve at a small strain corresponded to a realistic stress–strain curve; this completed the definition of the Eyring process. The product $C_X n_X$ was determined from the observed initial elastic response. The Ogden exponent n_X is defined as $n_X = 2m$, so, as established previously,[4] the overall response of the model in plane strain was similar to the response of the power-law flow

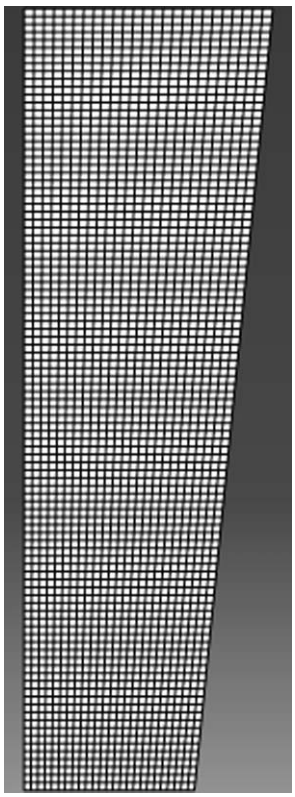

Figure 5 Finite element mesh for the quarter model of the tensile specimen of Figure 1(b).

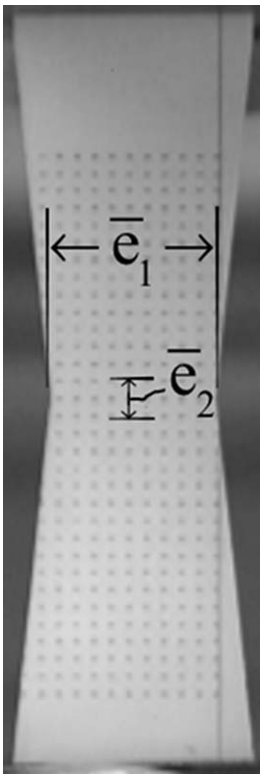

Figure 6 Image of the specimen showing the mean strain locations.

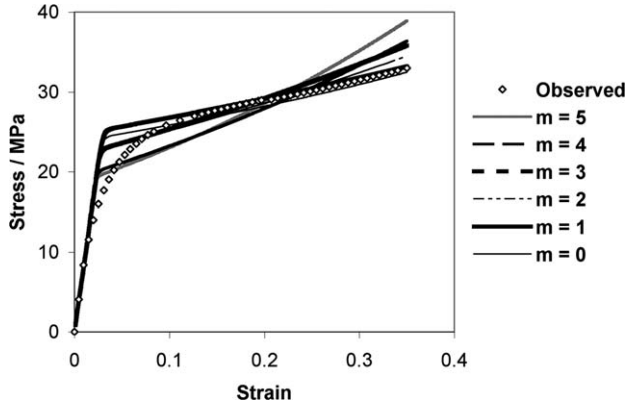

Figure 7 Model stress–strain curves in comparison with the observed curve for a strain rate of 0.018 s^{-1}.

rule. The parallel Ogden model in the hyperelastic arm was assumed to be Gaussian in nature, with $n_Y = 2$. Finally, the constant C_Y was determined such that the postyield stress response exhibited the appropriate degree of strain hardening. Each value of m was associated with a unique set of parameters, which are listed in Table I.

When modeling the uniaxial tension with the flow rule with $m > 0$, the plastic strain rate along the tensile stretching axis decreases as the strain increases; this is clear from an inspection of eqs. (10) and (12). This leads to an increase in stress with deformation postyield. As a result, this model can show strain-hardening behavior without the action of the network in the hyperelastic arm; the series Eyring/Ogden combination arm can exhibit strain hardening by itself. As a result, the values required for C_Y decrease as m increases. When $m = 5$, a value for C_Y of zero is associated with strain hardening at a higher level than observed. For this reason, we did not explore values of m greater than 5, as the predicted strain hardening would then be unreasonably high.

In Figure 8, we show the development of R with time as observed experimentally and as predicted with the finite element model of Figure 5 for values of m up to 5. Only times of 5 s or more are included, as at shorter times, the strains were too small to give good accuracy for the imaging method used. The upper limit of the time axis was set by the range of strain ($\leq$0.35) covered experimentally. For values of m between 0 and 3, the deformation predicted by the model changed unsystematically between stable and unstable, with the latter associated with highly localized strain (necking) at the specimen center. As is well established,[13–15] the strain rate sensitivity, essentially the quantity g in eq. (24), controls the stability of deformation, with high values tending to suppress necking. High values of m are associated with high values of g, and this is consistent with the stable deformation predicted for $m = 4$ and $m = 5$. However, lower values, $m = 0$ and $m = 2$, are associated with stable deformations whereas $m = 1$ and $m = 3$ are associated with necks beginning to form. In this range of m, small changes in the input data could switch the behavior between stable and unstable regimes. Figure 9 shows the states of deformation for values of m of 0, 1, 3, and 5. The general picture that emerged was that $m = 4$ and $m = 5$ gave predictions of deformation that were reasonably consistent with the experiments, whereas for the lower values, the deformation fields were quantitatively or qualitatively incorrect. This showed that the accuracy of the stress–strain curve was one of a number of considerations that are relevant in the assessment of a constitutive model. The accuracy of the strain rate sensitivity is in some cases more important, as it controls the stability of the deformation.

Some physical interpretation of the constitutive model was possible. It can be envisaged as comprising two parallel arms, one consisting of an Eyring model in series with an Ogden model (the combination arm) and the other consisting of a single Ogden model (the hyperelastic arm). The hyperelastic arm resembles the entropic component that is frequently included in models of polymers, as pioneered by Haward and Thackray,[16] and is associated with strain hardening at higher strains. In this study, we observed that the Eyring process in the combination arm of the model could also be a source of strain hardening via the flow rule when the exponent m exceeded zero. This was equivalent to a fall in the activation volume associated with deformation along the stretch direction. The idea that strain hardening may be both entropic in origin and also the result of falling activation volume has been suggested previously, and models have been proposed in which the activation volume falls as a function of strain.[17–19] However, a simple decrease in activation volume

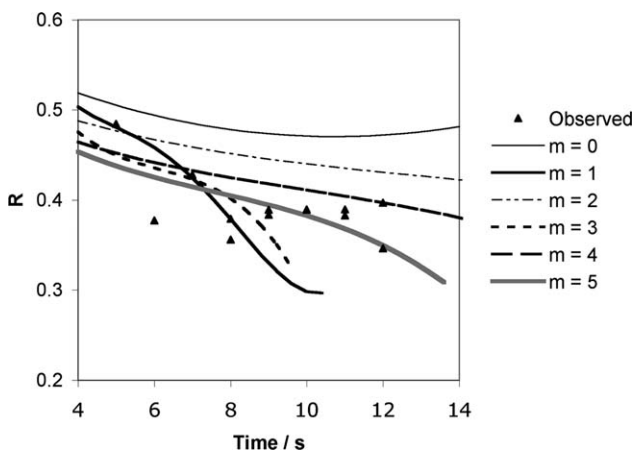

Figure 8 Evolution of the strain ratio (R) with time.

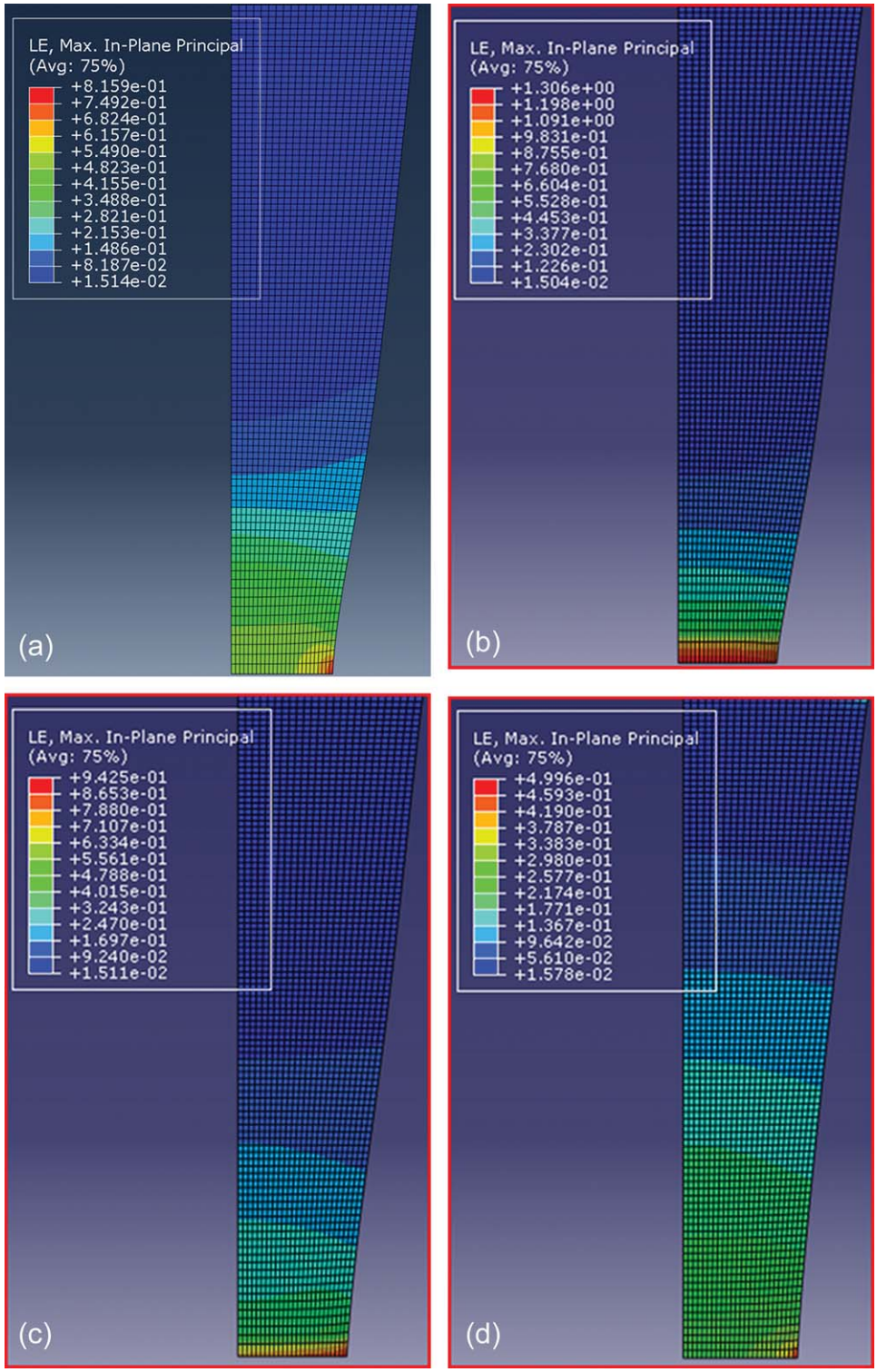

Figure 9 Strain field (LE = maximum principal strain) at 9.7 s for m = (a) 0, (b) 1, (c) 3, and (d) 5. [Color figure can be viewed in the online issue, which is available at wileyonlinelibrary.com.]

would affect the plastic strain rate in all directions indiscriminately; this would be unrealistic for the prediction of plastic strain rates in an arbitrary direction in an oriented polymer. This approach, in which the effect is included via the flow rule, is better justified. It is equivalent to the introduction of an activation volume that is tensorlike rather than a single value.

CONCLUSIONS

The flow rule introduced previously for modeling the compressive behavior of UHMWPE[4] was applied to the tensile behavior of the same material. It showed implications for the strain rate dependence of the stress, which were confirmed experimentally. This took the form of the dependence of the strain rate sensitivity on the strain; the experimental observations led to a power-law exponent m in the flow rule of approximately 5. In experiments involving inhomogeneous tensile strain fields, the plastic strain rates in the axial and transverse directions were predicted to be related in a way that depended on m. Observations of strain in these circumstances showed that the ratio of perpendicular strains was consistent with a value of m of 5.

As shown by both this study and a previous study on compressive behavior,[4] the analysis and observation of nonuniaxial strain fields were essential steps in the evaluation of constitutive models for UHMWPE. Generally, valid constitutive models are only possible when the strain-induced anisotropy is taken into account.

References

1. Sobieraj, M. C.; Rimnac, C. M. J Mech Behav Biomed 2009, 2, 433.
2. Bischoff, J. E Mech Time-Depend Mat 2008, 12, 189.
3. Avanzini, A. Mater Des 2008, 29, 330.
4. Sweeney, J.; Naz, S.; Coates, P. D. J Appl Polym Sci 2009, 111, 1190.
5. Kurtz, S.m/.; Muratoglu, O. K.; Evans, M.; Edidin, A. A. Biomaterials 1999, 20, 1659.
6. Figiel, L.; Buckley C. P. J. Non-Linear Mech 2009, 44, 389.
7. Buckley, C. P.; Jones, D. C. Polymer 1995, 36, 3301.
8. Spathis, G.; Kontou, E. Polym Eng Sci 2001, 41, 1337.
9. Hill, R. The Mathematical Theory of Plasticity; Oxford University Press: Oxford, 1985; Chapter 12.
10. Lekhnitskii, S. G. Theory of Elasticity of an Anisotropic Body; MIR: Moscow, 1981; Chapter 1.
11. Ward, I. M.; Sweeney, J. An Introduction to the Mechanical Properties of Solid Polymers, 2nd ed.; Wiley: Chichester, England, 2004; Chapter 10.
12. Naz, S.; Sweeney, J.; Coates P. D. J Mater Sci 2010, 45, 448.
13. Hart, E. W. Acta Metall 1967, 15, 351.
14. Coates, P. D.; Ward, I. M. J Mater Sci 1980, 15, 2897.
15. Sweeney, J.; Shirataki, H.; Unwin, A. P.; Ward I. M. J Appl Polym Sci 1999, 74, 3331.
16. Haward, R. N.; Thackray, G. Proc R Soc A. 1968, 302, 453.
17. Hope, P. S.; Ward I. M., Gibson A. G. J Mater Sci 1980, 15, 2207.
18. Hope, P. S.; Ward, I. M. J Mater Sci 1981, 16, 1511.
19. Ward, I. M. Polym Eng Sci 1984, 24, 724.